Lattice density functional theory investigation of pore shape effects. I. Adsorption in single nonperiodic pores

A. P. Malanoski and Frank van Swol
Department of Chemical and Nuclear Engineering, University of New Mexico, Albuquerque, New Mexico 87106
and Sandia National Laboratories, Albuquerque, New Mexico 87185
(Received 13 June 2002; published 10 October 2002)

A fully explicit in three dimensions lattice density functional theory is used to investigate adsorption in single nonperiodic pores. The effect of varying pore shape from the slits and cylinders that are normally simulated was our primary interest. A secondary concern was the results for pores with very large diameters. The shapes investigated were square pores with or without surface roughness, cylinders, right triangle pores, and trapezoidal pores. It was found that pores with very similar shape factors gave similar results but that the introduction of acute angled corners or very large side ratio lengths in rectangular pores gave results that were significantly different. Further, a rectangular pore going towards the limit of infinite side ratio does not approach the results of a slit pore. In all of these cases, the importance of features that are present for only a small portion of the pore is demonstrated.

DOI: 10.1103/PhysRevE.66.041602 PACS number(s): 68.43.−h, 64.70.Fx, 02.50.Ng

I. INTRODUCTION

The adsorption behavior of single pores has been studied extensively via simulation. Capillary condensation and prewetting of surfaces has been studied, as well as the influence of including ends on the pores [1–10]. Most of this work has been done for a few ideal geometries, such as slit and cylindrical pores. It is worthwhile to study the effect of varying the pore shape, something which has not been addressed in the literature, to see if this variation from ideal geometries results in a theoretical calculation that agrees better with the experimental work. This work is in part motivated by a recent experimental system that was determined to be straight noninterconnected pores with one or two openings [11–13]. There have been many studies of adsorption in mesoporous to nanoporous materials [14,15], and one issue in these experimental systems is the presence of pore connectivity of which the exact nature of is often not known. Many of these materials are prepared as powders and the effect of the orientation and packing of the individual powder particles on the adsorption is also not known; this does not prevent one from modeling these substances, although these factors present additional complications.

The work of Coasne *et al.* [12] on mesopores in silicon is one of the few examples where the pores were determined not to have interconnections, as the material was formed as a wafer rather than as a powder. These experimental results provide an excellent way to evaluate the accuracy of theoretical methods predicting adsorption in single pores, as this group has been able to characterize the pore distribution and has some measure of the variation in pore shape. In their system, the pore shapes do not correspond to any of the simple geometries used in previous simulation work, and the pore sizes are much larger than those usually studied in simulations. Using existing independent pore models of the ideal geometries, the calculated adsorption isotherm does not agree with the experimental data. In order to calculate results to compare with the experimental work, collections of pores or the individual pores need to be studied. The obvious benefit of studying individual pores is that the adsorption for many distributions can be computed from the same set of individual pores. In this work we study the variation seen in the adsorption behavior of single pores with changes in pore shape and size. In the following [16] paper, the results for pore distributions based on these pores are discussed. It should be noted that density functional theory calculations do not give a true hysteresis loop with a kinetic time-dependent component but rather show the maximum stability of each phase. In other studies, it has been shown that the hysteresis loops generated by considering the thermodynamic metastability of the phases give results that are very similar to the experimentally determined hysteresis loops.

II. MODEL AND METHOD OF SOLUTION

A three-dimensional single occupancy lattice density functional model was used to study the adsorption behavior in the various pore shapes. The model allows for a mean field square-well-type attraction for nearest neighbor sites on a lattice. For this study, a simple cubic lattice was used. The grand potential functional of M lattice sites and l species is represented by the following expression:

$$\beta\Omega[\rho]=\sum_{i}^{M}\left[\left(1-\sum_{k}^{l}\rho_i^k\right)\ln\left(1-\sum_{k}^{l}\rho_i^k\right)+\sum_{k}^{l}\left(\rho_i^k\ln\rho_i^k+\rho_i^k(\beta V_i^k-\beta\mu_i^k)+\frac{\beta}{2}\sum_{m}^{N}\sum_{n}^{l}\phi_{d(i,m)}^{kn}\rho_i^k\rho_{I(i,m)}^n\right)\right], \tag{2.1}$$

where ρ_i^k is the density of species k at lattice site i, β is $1/kT$ where T is the temperature and k is Boltzmann's constant, V_i^k is the external potential acting on species k at lattice site i, μ_i^k is the chemical potential of species k at lattice site

i, and N is the number of interacting neighbors for the chosen lattice (which in the case of a simple cubic lattice is 6). The attractive contribution was summed over only the interacting neighbors because these positions are the same for every site, which naturally leads to a very efficient and straightforward algorithm. The actual lattice site that is neighbor m of lattice site i is required in order to get the density of that neighbor; the function $I(i,m)$, which is dependent on the lattice used, gives this value. Although we restricted the interaction to only nearest neighbors, the functional has been written so that the interactions could extend to other distances and vary with the distance. This is done by using an interaction energy $\phi^{kn}_{d(i,m)}$, of species k with species n which depend on the distance $d(i,m)$ between lattice site i and neighbor m. In the algorithm, the value of $\phi^{kn}_{d(i,m)}$ is tabulated as there are only a few relevant distances and this is more efficient than repeatedly computing the function. Wall sites could have been treated as an individual species but it is more practical to calculate the interaction of all the wall sites with each individual lattice site for each species and add that to βV^k_i for that lattice site. The wall-fluid interactions are then calculated only once during the solution of the grand potential functional.

The partial derivatives with respect to the species density at each site can be determined from the grand potential functional

$$\frac{\partial \beta\Omega[\rho]}{\partial \rho^k_i} = \ln\rho^k_i - \ln\left(1 - \sum_i^n \rho^n_i\right) + \beta V^k_i - \beta\mu^k_i + \beta \sum_m^N \sum_n^l \epsilon^{kn}_{d(i,m)} \rho^n_{I(i,m)},$$

$$k = 1,l, \quad i = 1,S. \tag{2.2}$$

At equilibrium, all of these partial derivatives equal zero and Eq. (2.1) is at its global minimum. In practice, it is possible to solve for a local minimum rather than the global minimum of Eq. (2.1), depending on the initial density values assigned to all of the lattice sites. We interpret the local minima as metastable equilibrium points and use these to compute the adsorption and desorption branches to their maximum stability for this functional. A Picard iteration scheme was used to solve for the site densities at the specified chemical potential using the set of partial derivatives in Eqs. (2.2). Density functional theory is advantageous in this regard because the appropriate free energy is easily computed from Eq. (2.1) so that it is straightforward to determine which solution is the true (global) minimum from a selection of several minima generated from different initial conditions.

The adsorption isotherms were determined by starting at a low or high value of the chemical potential with a uniform low or high initial site density, and then incrementing the chemical potential by a small amount, $\pm 0.01kT$. After the initial chemical potential, the density profile from the previous value of the chemical potential was used as the starting profile at the current value. Some other branches were generated by starting a desorption run from a point on the adsorption curve before complete filling had occurred. During the generation of an isotherm, it was only necessary to compute the wall-fluid interactions once as they do not depend on changes in the chemical potential. This gives an added savings in computation cost.

We chose to use a model where the fluid-fluid interaction was present only for the nearest neighboring lattice sites. The critical temperature for this model is $kT_c = -\rho_c N \phi^{ff}_1/2$, where the critical density, $\rho_c = 0.5$, $\phi^{ff}_1 = -1.0$ is the mean field fluid-fluid attraction, and N is the number of sites that contribute ϕ^{ff}_1 to the interaction energy (which in this case is the lattice coordination number (6), which results in $kT_c = 1.5$). The simulations were run at a T/T_c of 0.583 which is similar to the value of the experimental work (0.609). The strength of the wall-fluid interaction was then tuned so that the adsorption behavior at low pressure values was qualitatively similar to the experimental behavior [12]. Qualitative agreement is sufficient to understand the trends that result from variations in pore shape. Also, since the nearest neighbor interaction is only qualitative, additional time was not spent on improving the model's prediction of low pressure adsorption behavior.

The wall-fluid interaction was modeled using a Lennard-Jones 12-6 potential rather than a square well, as these interactions were only evaluated once per isotherm. We used a cutoff of 6σ for this potential, where σ is the lattice site separation. Because this is a single occupancy model all fluids are approximated by spherical molecules, and in the case of nitrogen this implies $\sigma \approx 0.4$–0.5 nm. For this system we determined the wall-fluid interaction at which complete wetting occurs on a planar wall and found it to be $\epsilon_{wf}/\phi^{ff}_1 = 0.38$, where ϵ_{wf} is the interaction strength of the wall-fluid Lennard-Jones potential and ϕ^{ff}_1 is the mean field attractive interaction of the fluid with the fluid at a separation of 1σ. The value required to qualitatively reproduce the adsorption behavior at low pressures was $\epsilon_{wf}/\phi^{ff}_1 = 1.31$.

A variety of shapes was investigated that sample the most significant ways pore shapes may depart from a cylindrical shape; square, cylindrical, which can only be approximated on a simple cubic lattice, triangular, and rectangular pores with various aspect ratios which are defined as the ratio of one side length to the other. The square and triangular pores permit an examination of the influence of sharply defined corners at right and acute angles. The triangular and rectangular pores allow one to explore the influence of having the overall shape depart from a cylindrical shape. Cylindrical pores on the simple cubic lattice were constructed by choosing a center point and removing all complete lattice sites that were located inside a specified radius. 90° isosceles triangular pores were made by filling in half of a square pore along the diagonal.

III. RESULTS

One consideration when studying these pores is whether the pores are periodically infinite or are exposed to the bulk phase at their ends. Marconi and van Swol [6] have shown that the two cases result in very different desorption curves

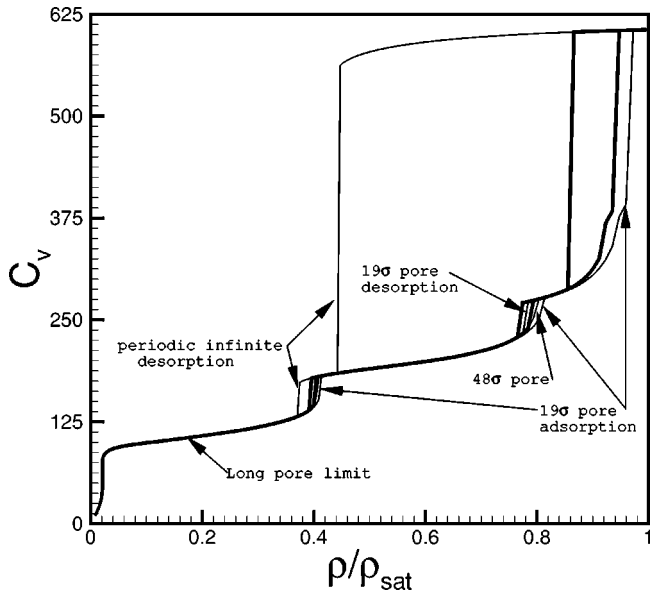

FIG. 1. Adsorption in the center slice C_v (625 max. value) versus saturation ρ/ρ_{sat} for square pores with a side length of 25σ [$C_v \equiv (\sigma/z_l)\int_{z'}^{z'+z_l}\int_a \rho(\vec{s},z)d\vec{s}dz$, see text]. Pores with ends are shown (19σ, 48σ, 68σ, 118σ, and 218σ) as well as the results for the periodic infinite pore. The three longest pores have identical adsorption and desorption curves (thick line). The adsorption of the periodic infinite pore is identical to the longer pore adsorption. The adsorption curves of the 19σ and 48σ pores are identical to the longer pore results except where noted.

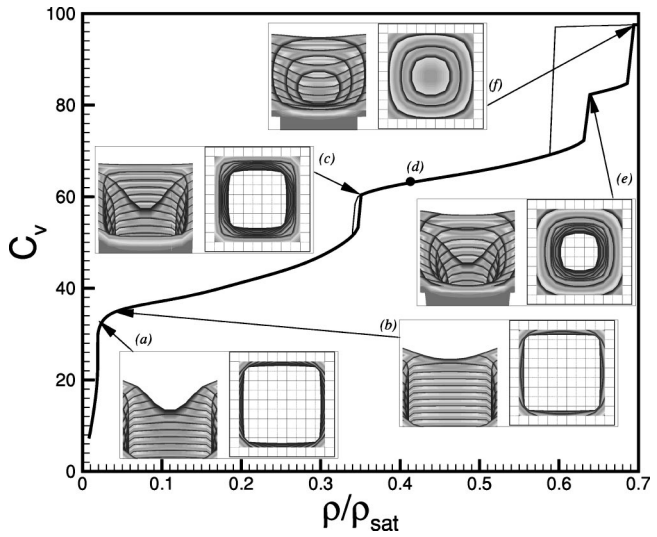

FIG. 2. Adsorption in the center slice C_v (see Fig. 1 caption) versus saturation ρ/ρ_{sat} for a square pore 10σ on a side. At points a,b,c,e,f 3D isodensity curvature plots are shown with contours drawn for densities greater than 0.4. The right view is straight down the pore axis and the left view is of the pore mouth seen from about 45 ° off the same axis.

for the pore. Since we are interested in the more physically realistic case, results were obtained for pores with ends unless stated otherwise. This introduces a problem because we are interested in pores where the ratio of the overall pore length to the pore diameter is very large (≈ 1000) and little of the length is associated with the openings [12]. Although feasible, actually modeling such pores would be very time consuming. We instead tracked the adsorption of an interior slice halfway through a pore that was sufficiently long.

In Fig. 1 we show the results for various pore lengths. The adsorbed material measured in each pore is $C_v \equiv (\sigma/z_l)\int_{z'}^{z'+z_l}\int_a \rho(\vec{s},z)d\vec{s}dz$ where a is the cross section of the pore, z' is the z coordinate for a position halfway through the pore length, $\vec{s}$ is a $2d$ vector, and z_l is one layer thick for pores without roughness and five layers thick for rough pores. The adsorbed material in the center slice, C_v, is plotted versus the saturation, defined as ρ/ρ_{sat}. The latter is defined as the density of the bulk fluid at a specified chemical potential and temperature divided by the density of the bulk fluid at the chemical potential at which the gas and liquid are in equilibrium and the same temperature. We have chosen to use the density saturation but it is equally valid to use the pressure saturation for which the adsorption, C_v, has the same behavior (the only difference is that transitions occur at slightly higher pressure saturations than density saturations).

For the shortest pore length, slight differences are seen for location of transitions relative to the longer pore lengths. This is due to the fact that the stability of a state point is dependent on the entire simulation volume, which varies with the pore length. For the second shortest pore (48σ), the capillary condensation loop matches the results of the longer pores, although some differences are still seen for the transitions at lower saturations. The adsorption curves are identical over the entire region for the longest pores (68σ, 118σ, and 218σ). The results for a periodically infinite pore are also shown. This pore has an *adsorption* curve which is identical to that obtained for the longer pore lengths with ends. The *desorption* branch is significantly different from the results for pores with ends [6].

We have established for sufficiently long pores that the adsorption in the center of the pore length does not depend on the pore length, and the adsorption in this center slice of the pore measures the total adsorption in pores with very long lengths. In reality there is a slight dependence on pore length as the adsorption behavior in the slice exponentially approaches a limiting value as the distance from the pore mouth increases. Based on these results, all pores studied in this work used a pore length of 68σ and have a separation of 32σ between the pore openings unless otherwise noted. In order to have sufficient exterior surface area and to ensure the pore studied was independent and not interacting with an image of itself, the walls that formed the pore walls were at least 18σ thick. We have chosen in this paper to only report C_v curves that result from adsorption or desorption; it is straightforward to determine where the equilibrium transitions occur but we stress that these depend on the entire pore including the exterior surface. These equilibrium transitions do show a small dependence on the pore length for all the pore lengths we have considered.

In Fig. 2 C_v is plotted versus the saturation ρ/ρ_{sat} for the adsorption and desorption isotherms of a square pore with a

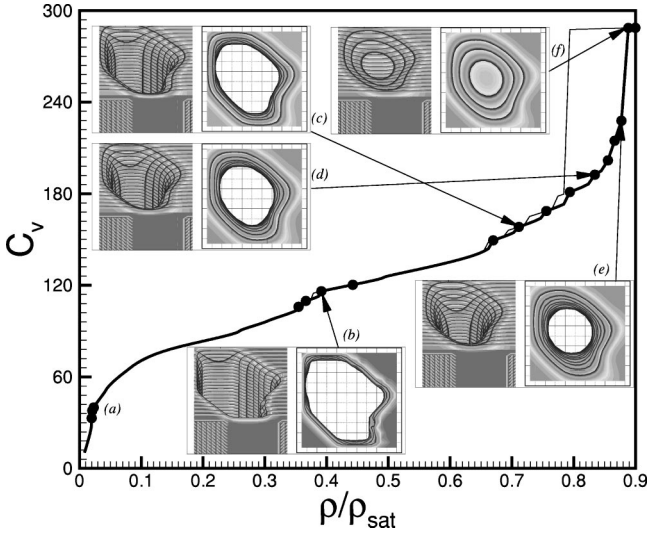

FIG. 3. Adsorption in the center slice C_v (see Fig. 1 caption) versus saturation ρ/ρ_{sat} for an arbitrary pore with acute, right, and obtuse angled corners where the largest side separation is 20σ. Points b,c,d,e,f 3D isodensity curvature plots are shown with contours drawn for densities greater than 0.4. The right view is straight down the pore axis and the left view is of the pore mouth seen from about 45 ° off the same axis.

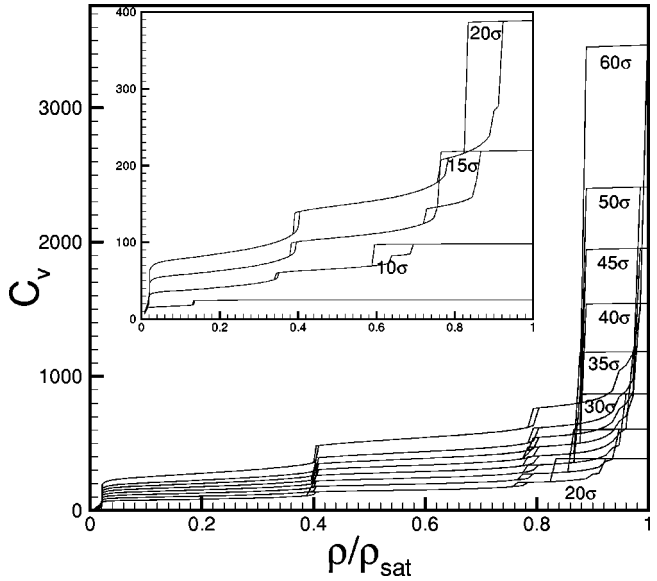

FIG. 4. Adsorption in the center slice C_v (see Fig. 1 caption) versus saturation ρ/ρ_{sat} for a series of square pores ranging in side length from 5σ to 60σ.

10σ side length. Also shown in Fig. 2 are three-dimensional (3D) isodensity plots at certain points of the isotherm for densities greater than 0.40. The walls are not drawn in these views. The right-hand view is straight down the axis of the pore, and the left-hand view is of the pore mouth viewed from about 45 ° off this axis. The points were taken from the adsorption isotherm because a desorption isotherm started from these points would not retrace the adsorption isotherm. The first jump around a saturation of 0.02, point *a*, is associated with a quasi-two-dimensional vapor-fluid transition, as the temperature these systems were run at is below the two-dimensional (2D) critical temperature. From the left-hand view, one can see that a 2D menisci formed on each wall at the pore mouth. At point *b*, the curvature of these menisci changes. At a saturation around 0.4, points *c*, a layering transition occurs and the liquid film on the walls of the pore suddenly increases in thickness. Comparing the left views of points *c* and *a*, one observes that the curvature of the film is very similar and only the thickness of the films differs. At point *d* (not shown), a curvature change is observed from point *c* that is similar to that seen upon going from point *a* to point *b*. At point *e*, another layering transition is observed. Finally at point *f*, the entire pore capillary condenses. From the left view of point *f*, one notes that a 3D meniscus has now formed. There are more transitions after this point (data not shown) which are associated with layering on the exterior planar surface of the pores. During these transitions, the 3D meniscus over the pore reduces in curvature and disappears when a thick enough film forms on the exterior surface.

In Fig. 3 we consider the case of a more arbitrarily shaped pore which contains acute, obtuse, and right angle corners. The walls not oriented along a lattice direction necessarily present a wall potential that varies near edges and over the whole wall on a very short length scale whereas the wall potential from walls along a lattice direction only varies near edges. The transitions around point *a* are not the formation of a complete thin film on all the pore walls but rather film formation at the acute angle corners. The film then forms reversibly as the saturation approaches point *b*. At the transitions around point *b* individual walls go through thickness changes. The transitions around points *c*, *d*, and *e* involve the formation of extra layers on the pore walls which again do not occur simultaneously for every wall. More material is adsorbed near the acute angle corners during these layering transitions, an effect which can be seen by viewing points *c*–*e*. The result of this adsorption behavior is that the variation in the curvature of the pore film is reduced as the saturation increases. Point *f* shows a view of the pore at capillary condensation.

In Fig. 4, C_v is plotted against the saturation ρ/ρ_{sat} of the adsorption and desorption curves for square pores ranging in side length from 5σ to 60σ. Fig. 4 demonstrates that a small absolute change in the pore size will result in a large change in the adsorption and desorption curves for small pore sizes. For large pore sizes, the adsorption and desorption curves appear to differ only by incremental amounts for a small change in pore size. Asymptotic behavior is seen for these pores (seen from the Kelvin equation). All of the pores have adsorption curves which show capillary condensation below the bulk saturation density. We note that a periodic bulk system solved via density functional theory has an adsorption curve that does not jump to the liquid phase until a saturation of 1.24, which is well beyond the equilibrium bulk saturation density. The general behavior of the other pore shapes as size increases is similar to that seen for the square pores. The presence and precise location of layering transitions is, of course, different from transition in square pores.

The influence of pore surface roughness in the square pores was explored by randomly inserting sites on the sur-

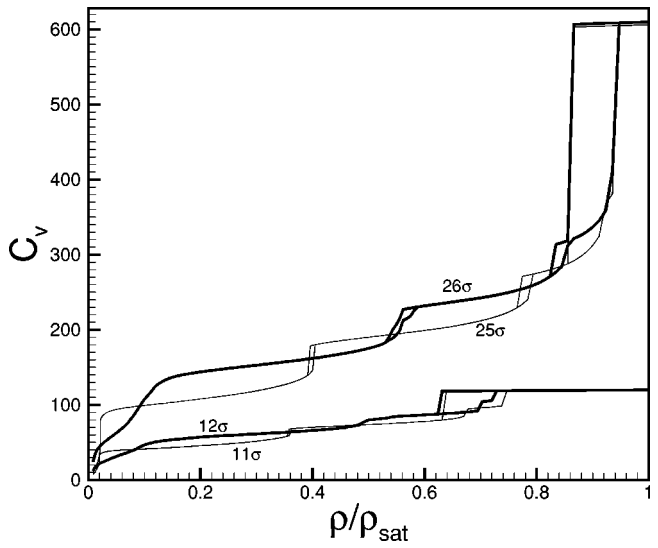

FIG. 5. Adsorption in the center slice C_v (see Fig. 1 caption) versus saturation ρ/ρ_{sat} for two smooth square pores (thin lines) and two square pores with surface roughness (thick lines).

face to give roughly 50% coverage. Figure 5 shows a comparison of C_v versus saturation ρ/ρ_{sat} for rough and smooth pores. C_v for the rough pores is the average of five cross-sectional slices in the center of the pore to sample the variation in roughness, compared to a single slice for the square pores whose surface does not vary. The key finding from this comparison is that the capillary condensation is largely unaffected by the introduction of surface roughness while the adsorption on the pore surfaces below the capillary condensation hysteresis loop is strongly affected. The layering transitions occur at higher saturations in the rough pore than in the smooth pore. This is because after the highly energetic sites of the roughened wall surface fill that wall surface effectively acts as a heterogeneous smooth wall that has a lower average wall-fluid interaction than a smooth wall consisting of wall sites only.

The best way to compare the results obtained for different pore shapes is not intuitively obvious. Two methods are to compare pores based on cross-sectional area or on circumference, which is the basis for comparison in BET calculations. Thus, one can compare two pore shapes with the same area or the same circumference. In Fig. 6 C_v is plotted versus the saturation, ρ/ρ_{sat}, for a square pore, two different rectangular pores, a triangular pore, and a cylindrical pore with roughly the same cross-sectional area, while in Fig. 7, we show the same square pore and the other shapes now with roughly the same circumference. Figure 6 also has an inset of the triangular pore's hysteresis loop compared with three different trapezoidal pores. Table I lists a quantitative measure of pore shape, C^2/A, where C is the pore circumference and A is the cross-sectional pore area. The differences in the trapezoidal pores of Fig. 6 are detailed in Table I. These figures show that pore shapes with roughly the same cross-sectional area give similar predictions for the hysteresis loop, although the adsorption behavior at lower saturations differs widely. The square pore and rectangular pore of aspect ratio 1.5 have the smallest differences in C^2/A compared to the cylinder

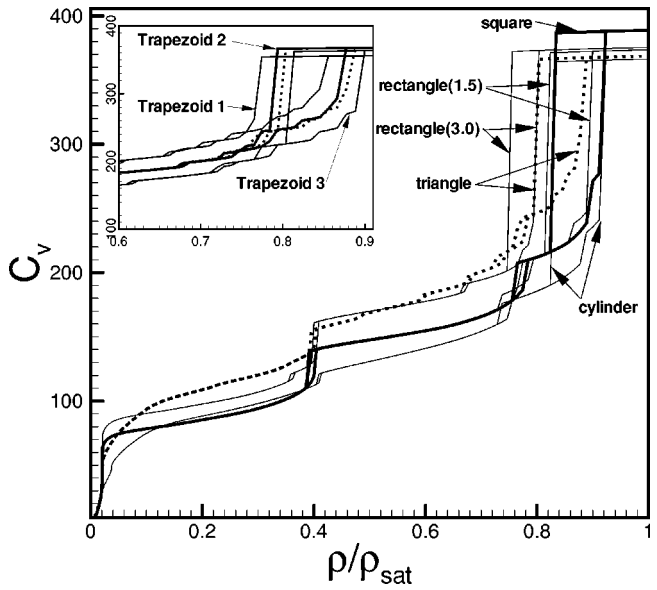

FIG. 6. Adsorption in the center slice C_v (see Fig. 1 caption) versus saturation ρ/ρ_{sat} for a 20σ square pore (thick line), a 23σ diameter cylindrical pore (thin line), a rectangular pore with a 1.5 aspect ratio and a 16σ short side (thin line), a rectangular pore with a 3.0 aspect ratio and a 11σ short side (thin line), and a right triangular pore with a 27σ short side (thick dotted line). The inset has a comparison of the hysteresis loop for the triangle pore compared to three trapezoidal pores (See Table I).

and this seems to be sufficiently small that roughly the same results are seen for these pore shapes. The triangular pore and rectangular pore with an aspect ratio of 3 display larger differences (Fig. 6). The triangular pore has a hysteresis loop

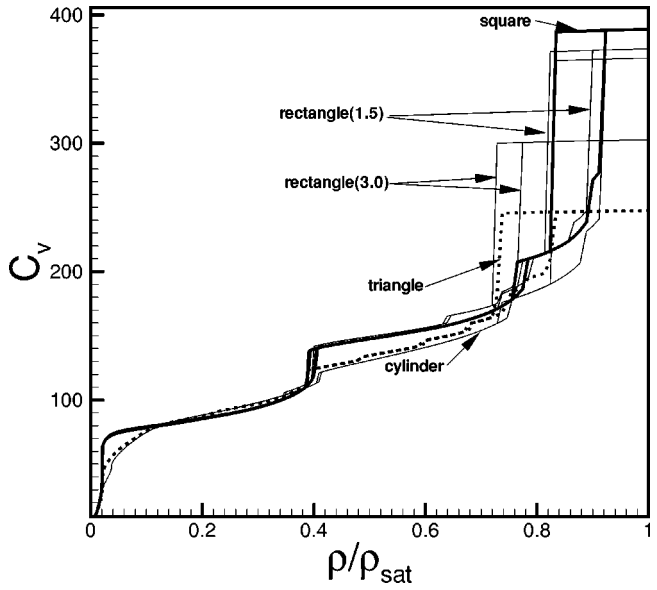

FIG. 7. Adsorption in the center slice C_v (see Fig. 1 caption) versus saturation ρ/ρ_{sat} for a 20σ square pore (thick line), a 23σ diameter cylindrical pore (thin line), a rectangular pore with a 1.5 aspect ratio and a 16σ short side (thin line), a rectangular pore with a 3.0 aspect ratio and a 10σ short side (thin line), and a right triangular pore with a 22σ short side (thick dotted line).

TABLE I. Area (A), circumference (C), and C^2/A for each pore shape.

Pore	Area (A)	Circumference (C)	C^2/A
Cylinder	πa^2	$2\pi a$	12.566
Square	a^2	$4a$	16
Right triangle	$a^2/2$	$(2+\sqrt{2})a$	23.314
Rectangle ($b=ha$)	$ba=ha^2$	$2(a+b)=2(1+h)a$	
Aspect ($h=1.5$)	$1.5a^2$	$5a$	16.667
Aspect ($h=3.0$)	$3a^2$	$8a$	21.333
Trapezoid	$(l-1/2+1)ha^2$	$(1+l+2\sqrt{h^2+(l-1)^2/4})a$	
(1) $h=8.33$, $l=25$	$108.333a^2$	$55.219a$	28.146
(2) $h=1$, $l=3$	$2a^2$	$(4+2\sqrt{2})a$	23.314
(3) $h=1.5$, $l=3$	$3a^2$	$7.606a$	19.284

which is shifted to slightly lower saturations, while the rectangular pore has a significant shift in the point where the hysteresis loop occurs. The trapezoidal pores in the inset demonstrate the same trends seen in the other pore shapes. Trapezoid 1 has the largest value of C^2/A and shows the largest shift to lower saturations. Trapezoid 2 has the same value of C^2/A as the right triangle and shows a hysteresis loop that almost matches the right triangle. Finally trapezoid 3 has the smallest C^2/A value and is the right most curve in the inset. The pores which contain acute angled corners (triangle and trapezoids) maintain a larger size of the hysteresis loop as C^2/A is increased compared to the rectangles.

The comparison based on circumference (Fig. 7) shows behavior opposite to the area comparison, with the low pressure adsorption curves in fairly good agreement but the hysteresis loops differing widely. The differences in the low saturation adsorption curves arise largely from differences in surface roughness and the angles formed in the corners. It should be noted that a rectangular pore with a ratio of 1.5 has roughly the same equivalent area and circumference as the square pore; this results in many of the transitions being identical. However, in some instances the layering transitions in the rectangular pore are broken into separate transitions for each side length. Figure 7 shows that the adsorption at low saturations can be predicted very well for any pore shape using a cylindrical pore with an equivalent circumference. Capillary condensation is more sensitive to pore shape, although for shapes which are not a large departure from an ideal cylindrical pore the results are similar. The pores whose shapes depart greatly from a cylindrical pore have a very different behavior and were investigated in more detail.

In Fig. 8 we show the behavior of rectangular pores with one side length fixed while the other is allowed to vary. If this varying side length were taken to infinity a slit pore with closed ends would be the result. The key feature of Fig. 8 is that after an initial shifting of the condensation hysteresis loop to higher saturations, some limiting value is rapidly reached which is not the hysteresis loop for the infinitely periodic slit pore. In fact, adsorption isotherms for slit pores do not condense until 10–15 % *above* the bulk saturation value at this temperature. Overall, the layering transitions observed at lower saturations for the rectangular pores do not appear in the slit pores until much higher saturation values are reached. From this we conclude that the presence of corners nucleates the layering transitions and pore filling in rectangular pores and surmise that this effect occurs in all close looped polygon pores. For rectangular pores, the shorter side length controls the maximum shift of the hysteresis loop to higher saturations. The hysteresis loop also shrinks in size before reaching some limiting value. It can be seen from the figures that a rectangular pore with high aspect ratio will not have a condensation hysteresis loop similar to a rectangular pore of the same cross-sectional area but much smaller aspect ratio unless the short side length itself is very large. As has already been noted, the differences between very large pores are much smaller and in most instances can be ignored.

The behavior of slit pores or planar surfaces may have an impact on the adsorption in these pores because we chose to study pores with ends opening onto an exterior surface. This exterior surface is flat except for the pore opening itself. Since we use periodic boundary conditions, the open spaces above each exterior surfaces are in fact a single region and

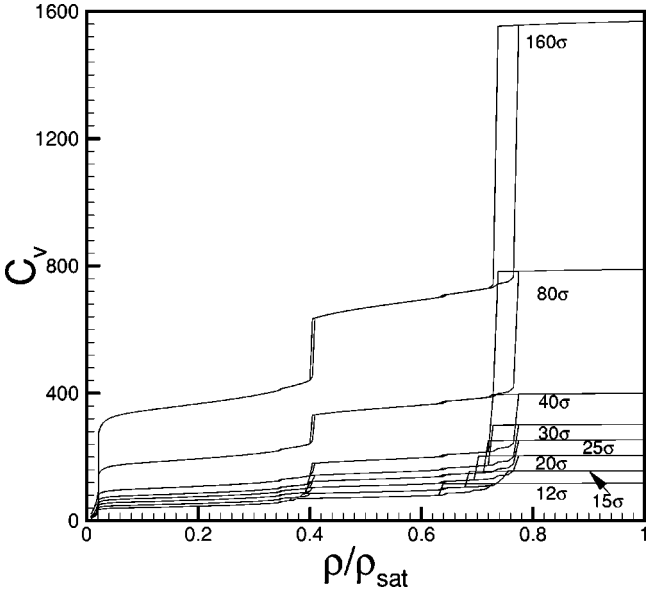

FIG. 8. Adsorption in the center slice C_v (see Fig. 1 caption) versus saturation ρ/ρ_{sat} for a series of rectangular pores with the short side fixed at 10σ. The long side length is noted in the figure.

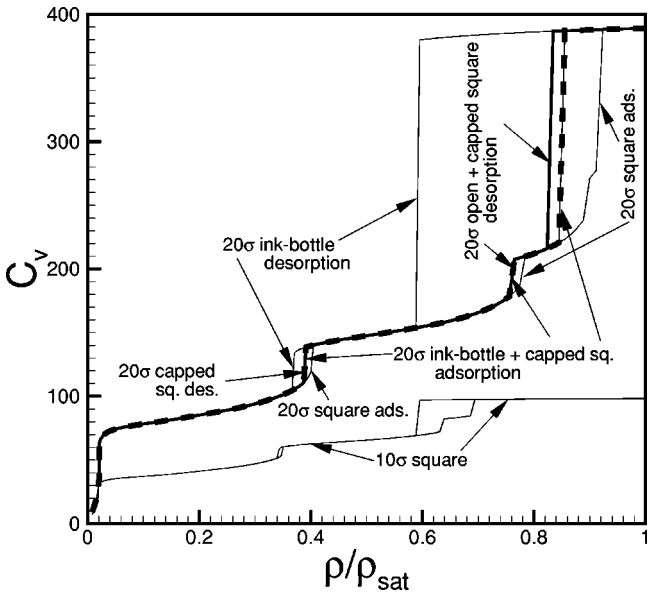

FIG. 9. Adsorption in the center slice C_v (see Fig. 1 caption) versus saturation ρ/ρ_{sat} for a square ink-bottle pore with 10σ necks and a 20σ body, adsorption (thick dashed line), and desorption (thin solid line). A 10σ square pore open at both ends is also shown (thin solid lines), as is a 20σ square pore with both ends open (thin solid lines), and a 20σ square pore with only one end open (adsorption—thin solid line, desorption—thick solid line).

this region is a slit pore after the pores are condensed. The wall potentials for these surfaces are not uniform but vary depending on whether one is over a wall site or a fluid filled pore. It is possible that a film on the exterior surface region could control the desorption of the pore. While a thick liquid film remains stable on the exterior surface, the pores have the properties of an enclosed pore (no openings) or an infinitely periodic pore. The desorption branch of such a pore, as seen in Sec. I, is stable to much lower saturations compared to the open pores where a meniscus forms at the pore opening. The requirement for a film on the exterior surface to control the desorption process is that the film must be sufficiently thick that menisci cannot form over the pores and must be stable to lower saturations than the open pore with a meniscus. For our model, a liquid film several sites thick, which could prevent the formation of menisci, persists during desorption on the surface of slit pores until a saturation of 0.9. The large pore emptying for the desorption curve takes place in this same region and may be controlled by this exterior film. For smaller pores, the exterior surface will not play a role since the thick liquid layer does not persist to low enough values of the saturation.

Because real pores may have a significant variation in their pore diameter down the length of the pore, we considered the adsorption in an ideal pore which exhibits such behavior. We considered ink-bottle-type pores where the ends in contact with the outside have smaller pore diameters (necks). In Fig. 9 C_v versus the saturation ρ/ρ_{sat} is shown for two straight square pores with side lengths of 10σ and 20σ and a square ink bottle with a neck side length of 10σ, a length from pore opening to the larger pore region of 19σ, a large region side length of 20σ, and a length from neck to neck of 100σ. The larger straight pore (20σ) is shown with both ends open and with one opening plugged. The desorption curve of the smaller straight pore gives a very good approximation of when the ink bottle pore empties. The adsorption curve of the ink bottle is similar to the large straight pore open at both ends except that any transitions showing hysteresis occur sooner in the ink bottle than in the straight pore. The adsorption for the straight pore with one end open is exactly that of the ink bottle pore. One may think this is a reasonable expectation as the ink bottle with the necks capillary condensed would appear to be a pore with a bottom. However, the transitions in the ink bottle at saturations well below the capillary condensation of the neck region are also shifted to lower saturations. At these transitions, the ink bottle pore still exhibits a hysteresis loop while the pore with one end open does not have a loop for any of these transitions. In general, pores open at one end do not have hysteresis loops (except for the pore filling) and when they do these loops are much smaller in size compared to pores open at both ends. Although smaller in size, a shift in the location of transitions to lower saturation is also seen in pore shapes where three walls meet in an acute angle, just as a shift in the location of transitions is seen for pores without corners (slits) to pores with corners. In general, the adsorption curve of the ink bottle pore will match that of the straight pore with one end open.

IV. CONCLUSIONS

An examination of nonideal shaped pores has revealed some interesting behavior as well as emphasizing some known features of these systems. It has been shown that for pores with shapes close to that of a cylinder, the capillary condensation in a cylinder pore of equivalent pore area will be similar to that of a pore whose shape is not cylindrical. For pores with a larger departure in shape (triangle, trapezoid, and rectangle of aspect ratio (3) the results are not as well predicted. If the adsorption at saturations below the saturation of the capillary condensation is of interest, a cylinder pore of equivalent circumference predicts the adsorption quite well. For pores with much larger aspect ratios and with a shorter length that is not too large, a departure from this behavior is seen and pore condensation occurs close to that of a cylinder with the shorter length as the diameter. For very large pores, the details of the shape and even the exact size of the pore is no longer important in determining the adsorption hysteresis loop. The presence of corners formed by the intersection of two pore walls helps to nucleate layering transitions in pores so that the layering observed for a planar surface will be seen in pores at much lower saturations. A similar but much smaller shift is seen in pores where three walls meet in an acute angles. It is important to note that features that affect only a small portion of the pore, such as the presence of pore openings, acute angled corners, and neck constrictions in ink bottle pores, have a significant impact on the adsorption-desorption curves and hysteresis of the entire pore.

[1] L. H. Cohan, J. Am. Chem. Soc. **60**, 33 (1938).
[2] L. H. Cohan, J. Am. Chem. Soc. **66**, 98 (1944).
[3] M. J. De Oliveira and R. B. Griffiths, Surf. Sci. **71**, 687 (1978).
[4] E. Bruno, M. B. Marconi, and R. Evans, Physica A **141**, 187 (1987).
[5] P. C. Ball and R. Evans, Langmuir **5**, 714 (1989).
[6] U. Marini Bettolo Marconi and F. van Swol, Phys. Rev. A **39**, 4109 (1989).
[7] M. W. Maddox, J. P. Olivier, and K. E. Gubbins, Langmuir **13**, 1737 (1997).
[8] A. V. Neimark, P. I. Ravikovitch, M. Grun, F. Schuth, and K. K. Unger, J. Colloid Interface Sci. **207**, 159 (1998).
[9] W. W. Lukens, Jr., P. Schmidt-Winkel, D. Zhao, J. Feng, and G. D. Stucky, Langmuir **15**, 5403 (1999).
[10] A. V. Neimark, P. I. Ravikovitch, and A. Vishnyakov, Phys. Rev. E **62**, 1493 (2000).
[11] B. Coasne, A. Grosman, C. Ortega, and M. Simon, in *MRS Symposium Proceedings, Dynamics in Small Systems V*, edited by J. M. Drake, J. Klafter, P. Levitz, R. M. Overney, and M. Urbakh (Materials Research Society, Warrendale, PA, 2001).
[12] B. Coasne, A. Grosman, N. Dupont-Pavlovsky, C. Ortega, and M. Simon, Phys. Chem. Chem. Phys. **3**, 1196 (2001).
[13] B. Coasne, A. Grosman, C. Ortega, and M. Simon, Phys. Rev. Lett. **88**, 256102 (2002).
[14] M. Jaroniec, M. Kruk, and J. P. Olivier, Langmuir **15**, 5410 (1999).
[15] B. Smarsly, C. Goltner, M. Antonietti, W. Ruland, and E. Hoinkis, J. Phys. Chem. B **105**, 831 (2001).
[16] A. P. Malanoski and Frank van Swol, following paper, Phys. Rev. E **66**, 041603 (2002).